RESEARCH ARTICLE

Key Points:
- Zonal and meridional variations of three-dimensional eddy structures are investigated in the Northwestern Pacific Ocean
- A new method is proposed to estimate the spatial distributions of eddy heat and salt transports in a Lagrangian framework
- Negative/positive divergence of eddy heat transport north/south of the KE suggests a poleward eddy heat transport across the KE jet

Supporting Information:
- Supporting Information S1

Correspondence to:
D. Dong,
dongdide90@126.com

Mesoscale Eddies in the Northwestern Pacific Ocean: Three-Dimensional Eddy Structures and Heat/Salt Transports

Di Dong[1,2,3] (ID), Peter Brandt[3,4] (ID), Ping Chang[5,6,7] (ID), Florian Schütte[3], Xiaofeng Yang[8] (ID), Jinhui Yan[1], and Jisheng Zeng[1]

[1]South China Sea Institute of Planning and Environmental Research, SOA, Guangzhou, China, [2]University of Chinese Academy of Sciences, Beijing, China, [3]GEOMAR Helmholtz Centre for Ocean Research Kiel, Kiel, Germany, [4]Christian-Albrechts-Universität zu Kiel, Kiel, Germany, [5]Department of Oceanography, Texas A&M University, College Station, TX, USA, [6]Physical Oceanography Laboratory/CIMSST, Ocean University of China and Qingdao National Laboratory for Marine Science and Technology, Qingdao, China, [7]Department of Atmospheric Sciences, Texas A&M University, College Station, TX, USA, [8]State Key Laboratory of Remote Sensing Science, Institute of Remote Sensing and Digital Earth of Chinese Academy of Sciences, Beijing, China

Abstract The region encompassing the Kuroshio Extension (KE) in the Northwestern Pacific Ocean (25°N–45°N and 130°E–180°E) is one of the most eddy-energetic regions of the global ocean. The three-dimensional structures and transports of mesoscale eddies in this region are comprehensively investigated by combined use of satellite data and Argo profiles. With the allocation of Argo profiles inside detected eddies, the spatial variations of structures of eddy temperature and salinity anomalies are analyzed. The results show that eddies predominantly have subsurface (near-surface) intensified temperature and salinity anomalies south (north) of the KE jet, which is related to different background stratifications between these regions. A new method based on eddy trajectories and the inferred three-dimensional eddy structures is proposed to estimate heat and salt transports by eddy movements in a Lagrangian framework. Spatial distributions of eddy transports are presented over the vicinity of the KE for the first time. The magnitude of eddy-induced meridional heat (freshwater volume) transport is on the order of 0.01 PW (10^3 m^3/s). The eddy heat transport divergence results in an oceanic heat loss south and heat gain north of the KE, thereby reinforcing and counteracting the oceanic heat loss from air-sea fluxes south and north of the KE jet, respectively. It also suggests a poleward heat transport across the KE jet due to eddy propagation.

1. Introduction

The region encompassing the Kuroshio Extension (KE) in the Northwestern Pacific Ocean is one of the most eddy-energetic regions of the global ocean. As an energetic eastward flowing inertial jet, the KE is characterized and surrounded by a complicated ocean circulation structure (Figure 1b). The Oyashio flows from the north and forms the Kuroshio-Oyashio extension region (KOER; Itoh & Yasuda, 2010a) together with the KE (Isoguchi et al., 2006). Complex frontal structures such as the Subarctic Front, the Subarctic Boundary, and the Kuroshio Bifurcation Front are found in the east. The KE is flanked by anticyclonic and cyclonic recirculation gyres in the south and north, respectively. Among them is the Shikoku Recirculation Gyre in the Shikoku Basin south of the KE (Nagano et al., 2013), which is well expressed in sea level anomaly (SLA) data.

The KE sheds off vigorous mesoscale eddies toward north and south, which in turn interact with the fronts. Additionally, mesoscale eddies originating from the subarctic and subtropical Pacific move toward the KE region. All these eddies, with properties indicative of an origin from the KE, the Oyashio, the Tsugaru Warm Current, and the Sea of Okhotsk (Itoh & Sugimoto, 2001), contribute to the meridional heat and salt transport in the North Pacific, impacting the Kuroshio path (Ma et al., 2016; Miyazawa et al., 2004; Waseda, 2003), regional hydrography, water mass modification (Itoh & Yasuda, 2010b; Kouketsu et al., 2012), marine biology (Kouketsu et al., 2016; Kusakabe et al., 2002), fisheries, and even the overlaying atmospheric boundary wind, rain and storm tracks (Ma et al., 2015a, 2015b).

Mesoscale eddies in the KE region have been extensively investigated by hydrographic measurements from research vessels and autonomous platforms like Argo floats and gliders (Ebuchi & Hanawa, 2000; Itoh et al., 2014; Itoh & Yasuda, 2010b; Saitoh et al., 1998), infrared imagery, altimetry data (Ebuchi & Hanawa, 2000,
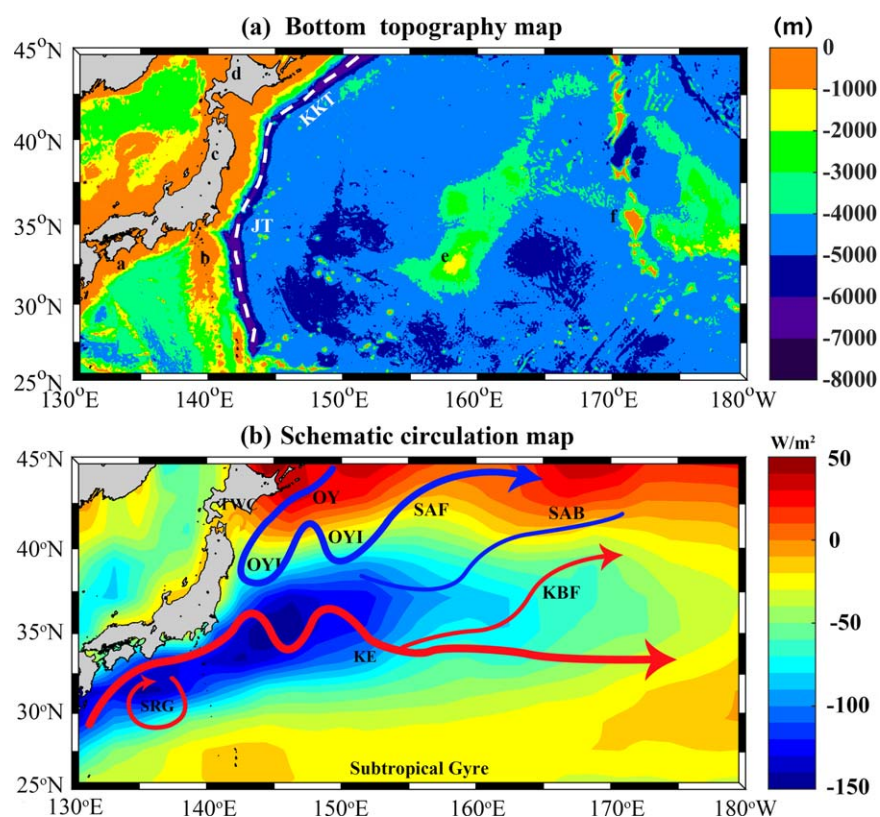
Figure 1. (a) Bottom topography map and (b) schematic circulation map in the Northwestern Pacific Ocean, the color shading in Figure 1b corresponds to the annual mean net surface heat flux from the NCEP-NCAR reanalysis data. Labels a–f in Figure 1a represents: a, Shikoku; b, Izu-Ogasawara Ridge; c, Honshu; d, Hokkaido; e, Shatsky Ridge; and f, Emperor Seamounts. The Kuril-Kamchatka Trench (KKT) and the Japan Trench (JT) are represented by white dashed lines. Circulation features shown in Figure 1b are the Oyashio current (OY), the Tsugaru Warm Current (TWC), the southward intrusion of the Oyashio (OYI), the Kuroshio Extension (KE), the Kuroshio Bifurcation Front (KBF), and the Shikoku Recirculation Gyre (SRG), the Subarctic Front (SAF), and the Subarctic Boundary (SAB).

2001; Itoh & Yasuda, 2010a), as well as model simulations (Tsujino et al., 2006) in the past 40 years. In the early years, researchers mostly relied on in situ measurements and infrared imagery to analyze the spatial distribution and evolution of warm-core and cold-core eddies, especially the warm anticyclonic eddies (AEs) north of the KE. With the availability of precise satellite altimeter data due to improved orbit control in the early 1990s, oceanographers started to use SLA or eddy kinetic energy (EKE) to investigate mesoscale activities in the KE. Ebuchi and Hanawa (2001) detected eddies in the Kuroshio recirculation region south of the KE with SLA data manually and found that the decay and movements of eddies are affected by bottom topography. Both the Okubo-Weiss (OW) parameter (Chelton et al., 2007) and a SLA-based automated eddy detection method (Chelton et al., 2011) have been used to detect and track eddies in the global ocean, but neither of them has made detailed analysis in the KE region. Itoh and Yasuda (2010a) presented the first quantitative description of the characteristics and movements of mesoscale eddies in the KOER based on altimetry data using OW parameter. They related eddy distributions to local topography and fronts and further analyzed water mass structures of the warm and cold eddies using Argo float data. Sasaki and Minobe (2015) focused on eddies shed from the KE based on a jet length change detection method and investigated their climatological characteristics and variability. As to those eddies, they roughly estimated the related eddy meridional heat transport across the KE jet to be about 0.023 PW. Waterman et al. (2011) studied eddy-mean flow interaction in the KE region with data collected by an array of tall current meter moorings, particularly focusing the discussion on the different sources of eddy variability such as jet meandering, ring formation, waves, and jet instability. More recently, Sun et al. (2017) investigated the vertical eddy structures within our study region (140°E–180°E, 28°N–40°N) and found significant seasonal variations of eddy-modulated mixed layer depth anomalies. However, Sun et al. (2017) studied neither the spatial

variations of eddy structures in the KE nor the eddy heat or salt transports. Thus, although a rich body of literatures exists about mesoscale eddies in the Northwestern Pacific Ocean, few studies have examined spatial variations of eddy structures and eddy-induced heat and salt transport there. The existing remote sensing data set of SLA, together with Argo float profiles makes it possible for us to further investigate the potential influences of Kuroshio eddies on the three-dimensional temperature and salinity fields of the upper ocean, and to estimate the eddy-induced meridional and zonal transports of heat and salt in the Northwestern Pacific Ocean, encompassing the KE region.

Eddy heat transport is traditionally estimated within an Eulerian framework (Qiu & Chen, 2005; Roemmich & Gilson, 2001; Stammer, 1998), which does not explicitly identify eddy movements. In a Lagrangian framework, Dong et al. (2014) combined an eddy data set derived from an automated eddy detection method, with Argo profiling float data to estimate global eddy heat and salt transports. Although they presented the eddy transport values in large ocean basins, point-to-point fluctuations and sampling errors did not allow them to present detailed spatial distribution maps of eddy-induced transports in the KE. On the other hand, Zhang et al. (2014) formulated a method to estimate eddy mass transport, but no heat or salt transports were obtained. In addition, most previous studies (Castelao, 2014; Chaigneau et al., 2011; Schütte et al., 2016) focused on regions where eddies dissipate to calculate the eddy-induced ocean heat gain or loss, based on the assumption that eddies release the heat and salt anomalies trapped in their cores when they dissipate. In this paper, we attempt to take into consideration the effects of eddy birth and death, as well as changes in mean eddy structures and background conditions along eddy paths, and finally compare the eddy-induced heat transport divergence/convergence with the air-sea surface heat fluxes.

The main objectives of this paper are (1) to calculate and analyze spatial variations of eddy structures in the Northwestern Pacific Ocean and (2) to investigate eddy heat and salt transports within a Lagrangian framework. The paper is organized as follows: section 2 provides details about the data and methods used in this study; section 3 investigates the impact of eddies on the thermocline and halocline and calculates heat and salt transports by eddy movements. Results are summarized and discussed in section 4.

2. Data and Methods

Our study region extends from 25°N to 45°N, from the Japanese coast to 180°E (Figure 1). The northern boundary is located south of the Bussol' Strait, where the East Kamchatka Current and the outflow of the Sea of Okhotsk meet and form the Oyashio (Yasuda et al., 2000). The southern boundary is located close to the center of the subtropical gyre of the North Pacific, characterized by high EKE (Yang et al., 2013).

2.1. Data

Mesoscale eddies were detected with the delayed-time reference data "two-sat-merged" SLA (version 2014), produced and distributed by the CMEMS (Copernicus Marine and Environment Monitoring Service) over the period from January 2000 to December 2014. The data are daily multimission altimeter products, resampled to a 0.25° × 0.25° spatial resolution, with respect to a 20 year mean sea surface height (1993–2012).

The vertical structures of mesoscale eddies were investigated with Conductivity-Temperature-Depth (CTD) profiles from Argo floats taken in the study region. The Argo data from January 2000 to December 2014 were provided by the Coriolis Global Data Acquisition Center of France, and downloaded from http://www.coriolis.eu.org. As the acquired Argo profiles were still suspicious (Chaigneau et al., 2011), a quality control is applied (see Appendix A for details). The final data set used in this study contains 49,482 profiles, corresponding to 33% of the total raw profiles. The distribution of Argo floats in the KE region is not homogenous: the western part, especially south of the KE, is intensively sampled; whereas in the east, the number of Argo profiles is fewer (Figure 2). To study the meridional and zonal variations of eddy structures, we divide the study region into nine subregions: 35°N is used to divide the region into the north and south of the KE; and to zonally separate the region, subregion boundaries at 140°E, 150°E, 160°E, and 170°E are used, resulting in nine 10° × 10° boxes, thereby neglecting the Sea of Japan. The number of profiles inside (separating AEs and cyclonic eddies [CEs]) and outside eddies are labeled in Figure 2.

To reveal the intensive air-sea interactions in the KE, the mean atmospheric net heat flux was derived from the long-term monthly means of the National Centers for Environmental Prediction-National Center for
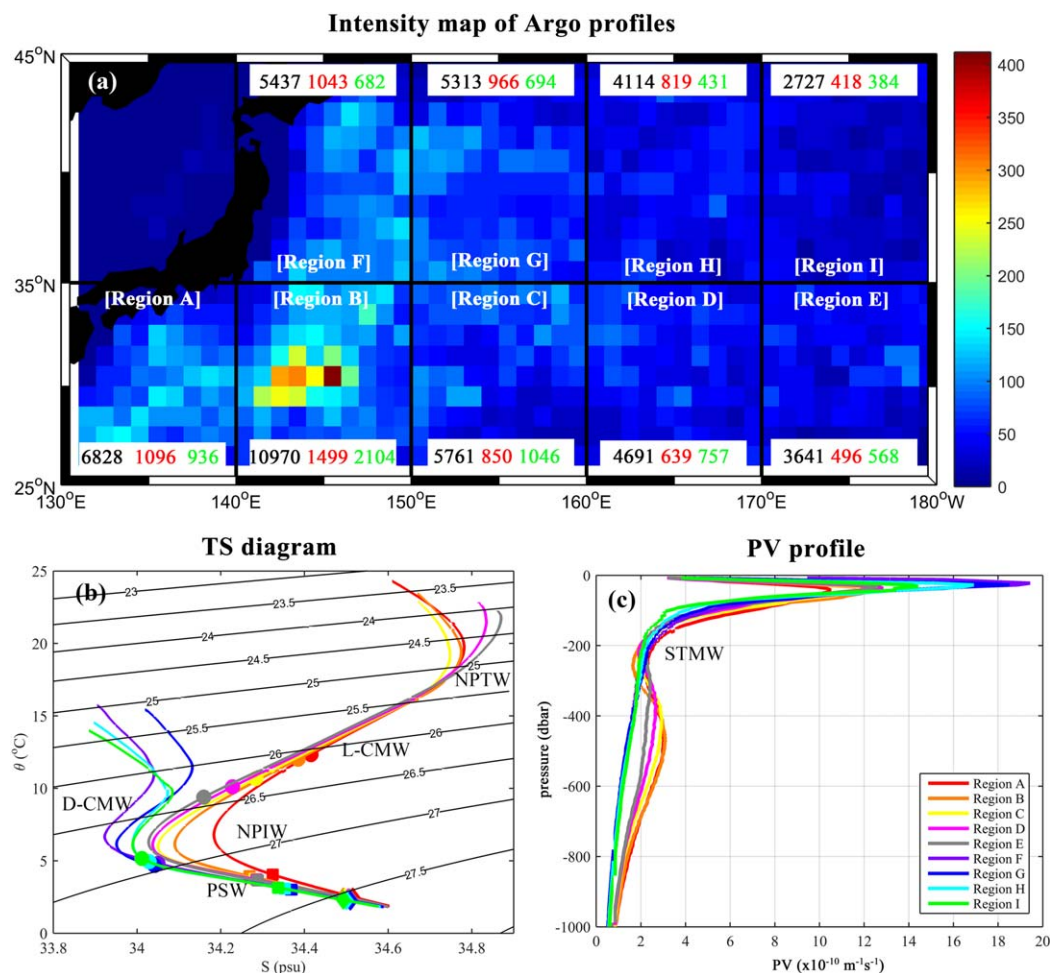
Figure 2. (a) Intensity map of available Argo float profiles in the Northwestern Pacific Ocean (the number of Argo float profiles in $1° \times 1°$ grid boxes in the period 2000–2014). The brackets denote the subregions A–I. The black, red, and green numbers in each subregion represent the profile numbers outside eddies, inside AEs, and inside CEs, respectively. (b) Mean potential temperature-salinity characteristics and (c) mean potential vorticity (PV) profiles for all subregions, calculated with all Argo float profiles outside eddies. The pressures of 500, 1,000, and 1,500 dbar are denoted by circle, square, and diamond markers in Figure 2b. The PV minimum in Figure 2c marks the depth range of the Subtropical Mode Water (STMW).

Atmospheric Research (NCEP-NCAR; Kalnay et al., 1996) reanalysis data during years 1981–2010, which has a spatial resolution of 2.5°.

To calculate the heat and salt transports by eddy movements, we use the "Mesoscale Eddy Trajectory Atlas" product. This data set is developed and validated in collaboration between CLS/DUACS and D. Chelton, distributed by AVISO+ in 2017, so we call it CH17 for short (see Appendix B for details). We also used the third version of eddy trajectories based on weekly SLA data from Chelton et al. (2011; CH12) for comparison and validation. Both data sets contain only mesoscale eddies with lifetime greater than 28 days.

2.2. Methods

Although the eddy data sets from Chelton et al. (2011) has been widely applied for eddy research in various oceans, no eddy boundary information is recorded, which makes it difficult to determine whether Argo floats are inside or outside a given eddy (even with given eddy radius, it is difficult to locate Argo floats in reference to eddies, because eddy shapes often deviate from being circular). To obtain the missing eddy boundary information, we used the eddy detection method of Faghmous et al. (2015; FAG). We then combined eddy trajectories from CH17 with FAG to formulate a new method to estimate eddy heat and salt transports. We also modified the approach by Zhang et al. (2014; MZ method), enabling it to estimate eddy

heat and salt transports, so that we can validate eddy heat and salt transport estimates using two different methods.

2.2.1. Eddy Detection Method

Mesoscale eddies were detected using the FAG method (Faghmous et al., 2015), which defines eddies as the outermost closed-contour SLA containing a single extremum (see Appendix C for details). Several criterions were applied when applying the FAG method to the daily SLA data in the KE region: a feature is treated as an eddy, only if its radius is larger than 35 km (Chelton et al., 1998; Schütte et al., 2016), its amplitude is larger than 1 cm, and it has only one extremum (defined as the eddy center; Chelton et al., 2011).

2.2.2. Three-Dimensional Eddy Structure

By colocating Argo float profiles and detected eddies in time and space, the eddy-induced potential temperature (θ) and salinity (S) anomalies (θ' and S', respectively) for each Argo profile inside of eddies is obtained by subtracting from the considered profile a local mean climatological profile computed by averaging all available θ and S profiles acquired outside eddies and within a spatial (temporal) radius of 200 km (30 days) from the position (date) of the considered profile (Castelao, 2014, Pegliasco et al., 2015).

To obtain the three-dimensional eddy-induced θ' and S' structures in a specific subregion, all anomaly profiles in that area are first accumulated, and the composite eddy structures are interpolated using a similar method as applied in Yang et al. (2013). All θ' and S' data are transformed onto an eddy-coordinate space and mapped onto 10 km × 10 km grids with the inversed distance weighting (IDW) interpolation. Also, at each depth level, anomaly data are treated as outliers and are deleted if they are more than 3 times away from either the first or the third quartiles. For each grid point, profiles with a radius of influence R = 60 km are assigned with a weight value $W_i = e^{-(d/R)^2}$ for interpolation. Here d is the distance between the profile and the grid point. The anomaly value of each grid point V_p is calculated from the Argo profiles V_i with $V_p = \sum W_i V_i / \sum W_i$. Thus for each subregion, one specific three-dimensional θ'/S' (300 km × 300 km × 2,000 m) eddy composite structure, or a 31 × 31 × 400 matrix can be obtained (the vertical resolution is 5 m).

2.2.3. A New Method for Heat and Salt Transports by Eddy Movements

To further consider the meridional variations of eddy structures for estimating eddy transports, we divide our study region (25°N–45°N, 130°E–180°E) into 20 subregions (5° latitude by 10° longitude) and calculate the mean three-dimensional eddy-induced θ' and S' for both AEs and CEs using all anomaly profiles taken within eddies in each of these subregions. To consider eddies which are born outside and transport into our study region, we enlarge the region (20°N–55°N, 130°E–170°E, excluding the Sea of Japan and the Sea of Okhotsk) to compute eddy structures. We divided the region south of 45°N into boxes of 5° in latitude by 10° in longitude; and the region north of 45°N into boxes of 10° in latitude by 10° in longitude (note that the number of Argo profiles is much smaller in the north), resulting in 30 subregions in total.

The eddy heat anomaly (H_e) and salt anomaly (S_e) can be obtained for each subregion:

$$H_e = \rho C_p \int_{-D_0}^{0} \int_{-X_0}^{X_0} \int_{-Y_0}^{Y_0} \theta' \, dx \, dy \, dz \tag{1}$$

$$S_e = \rho \int_{-D_0}^{0} \int_{-X_0}^{X_0} \int_{-Y_0}^{Y_0} S' \, dx \, dy \, dz \tag{2}$$

Here the mean upper ocean density and heat capacity are $\rho = 1,025$ kg m^{-3} and $C_p = 4,200$ J kg^{-1} °C^{-1}. θ' is the eddy-induced potential temperature anomaly, S' is the eddy-induced salinity anomaly, D_0 is the integration depth, X_0 and Y_0 are the x and y limits of the eddy structure boxes, respectively. Here we used $D_0 = 1,400$ m. According to Flierl (1981) and Chaigneau et al. (2011), an eddy is highly nonlinear when the ratio of its tangential velocity and its drift velocity exceeds 1. So a composite eddy can trap water within the depth range, where the tangential velocity is larger than its drift velocity. Using the same method as applied by Chaigneau et al. (2011), the average eddy "trapping depth" in the KE region is estimated at ~1,400 m.

Eddies may propagate long distances, thereby passing different subregions. Although coherent eddies trap water masses, they may also be modified by the background conditions or eddies (Itoh et al., 2014; Yang et al., 2013). We assume that each eddy can be characterized by an average heat and salt anomaly that depends on the time the eddy spends in the different subregions. We follow each eddy trajectory, and

apply the time it spends in one specific subregion as a weight to calculate the average heat anomaly for this eddy $H_{ea} = \sum t_i He_i / \sum t_i$, here t_i is the time the eddy spends inside region i, and He_i is the value of the specific eddy heat anomaly inside region i ($i = 1, \ldots, 30$). Similar procedures can be applied to calculate the average eddy salt anomaly, and the following steps are also the same for calculating eddy salt transport.

Instead of using eddy propagation velocity to calculate eddies' heat transport (Dong et al., 2014), we propose a new method which mainly uses eddy trajectories to calculate transport by eddy movements. As the resolution of SLA data is 0.25°, we use 0.25° × 0.25° grid cells. For each eddy, we follow its trajectory and check whether it crosses grid cell boundaries. Every grid cell has four boundaries. If an eddy crosses the western and eastern boundaries, it results in zonal heat transport across that boundary; whereas eddy crossing of the northern and southern boundaries results in meridional heat transport. In addition, the east and the north are defined as positive. So if one eddy crosses the east/west boundary from the west to the east, the heat transport is one multiplied by the specific eddy heat transport H_{ea}; if from the east to the west, the heat transport is minus one multiplied by the specific eddy heat transport H_{ea}.

For the north and south boundary of a grid cell, the meridional AE/CE heat transport $Q_k = \frac{\sum H_{eai}}{d_{lon} \cdot T}$ ($k = n, s$) is equal to the sum of heat anomalies of all AE/CE (with sign depending on the direction of the eddy trajectory), divided by the zonal length d_{lon} and time length T (unit: s) corresponding to the number of snapshots. As we choose CH17 data set based on the daily SLA data from 1 January 1993 to 31 December 2014, $T = 8,034 \times 24 \times 3,600$ s (8,034 is the number of snapshots during the whole 22 years, 24 is the hours for 1 day, and 3,600 is the seconds for 1 h). The zonal AE/CE heat transport is correspondingly $Q_k = \frac{\sum H_{eai}}{d_{lat} \cdot T}$ ($k = w, e$), where d_{lat} is the meridional length of the grid cell. For each grid cell, the meridional eddy heat transport is the average of heat transports at the northern and southern boundaries $Q_{mg} = (Q_n + Q_s)/2$. Likewise, the zonal eddy heat transport is the average of heat transports on the western and eastern boundaries $Q_{zg} = (Q_w + Q_e)/2$. Calculating grid by grid, we can obtain the eddy heat transport map for our study region. A moving average filter with 1.25° × 1.25° box size is applied to reduce noise.

After calculating eddy heat transports in the KE, the divergence of the heat transport Div_h in each grid can be calculated (unit: W/m^2):

$$Div_h = \nabla_h \cdot Q \qquad (3)$$

Here $Q = \begin{bmatrix} Q_x & Q_y \end{bmatrix}$ is the horizontal heat transport vector with the horizontal divergence, $\nabla_h \cdot$, taken over the grid cell of 0.25° zonal and meridional length. Then we calculate the ratio of the eddy-induced heat transport divergence relative to the atmospheric net heat flux in the KE.

Salt transport can be treated as an equivalent freshwater volume transport assuming conservation of mass across the transport section (Dong et al., 2014), so $F_{fw} = -Q_s / \rho_o S_o$, where $S_o = 35$ psu is the mean upper ocean salinity, Q_s is the time-mean salt transport by eddy movements. The unit of F_{fw} is m^3 s^{-1}.

3. Results

3.1. Three-Dimensional Eddy Structures

Before discussing eddy vertical structures, we first introduce the main water masses in the study region. As shown in Figure 2b, all the mean θ-S diagrams south of the KE show a reversed "S" shape, with two salinity extrema featuring two water masses: the subsurface high-salinity North Pacific Tropical Water (NPTW) and the low-salinity North Pacific Intermediate Water (NPIW, $\theta = 10$–$22°C$, S = 34.2–35 psu). The mean θ-S diagrams north of the KE also show a reversed "S" shape, having a salinity maximum (minimum) at the subsurface (intermediate) depth. The salinity minimum may be associated with the NPIW and the Transition Region Mode Water (TRMW, $\theta = 5.0$–$7.5°C$, S = 33.6–33.9 psu, $\sigma_\theta = 26.4$–26.7 kg/m^3; Kouketsu et al., 2012). South of the KE, NPIW becomes saltier as spreading westward from region E to region A, which is likely caused by intensive mixing. North of the KE, NPIW becomes fresher as spreading westward from region I to region F, due to the fresh intrusion from the Oyashio. Signatures of the low potential vorticity (PV) North Pacific Subtropical Mode Water (STMW, $\theta = 16.0$–$21.5°C$, S = 34.65–34.95 psu, $\sigma_\theta = 24.2$–25.6 kg/m^3) are evident south of the KE, especially in region B within a PV minimum between 200 and 350 dbar. Although the Lighter Central Mode Water (L-CMW, $\theta = 10.0$–$16.0°C$, S = 34.30–34.65 psu, $\sigma_\theta = 25.4$–26.3 kg/m^3) are reported to be generated mainly north of the KE (33°N–39° N), the θ-S curves for the region south of the KE
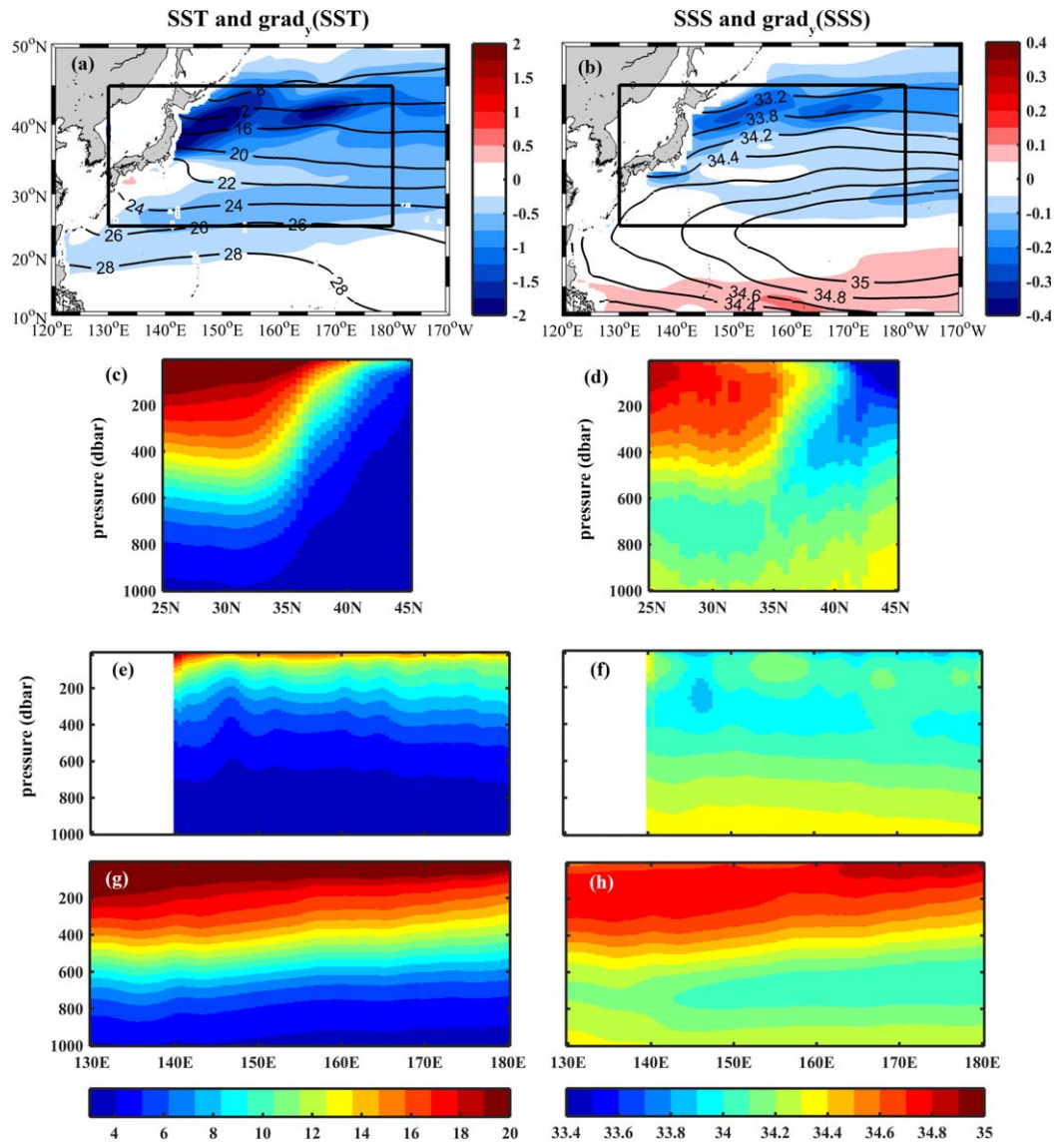
Figure 3. (a) Annual mean SST (contours) and its meridional gradient (color, °C/100 km) in the Northwestern Pacific Ocean. (b) Annual mean SSS (contours) and its meridional gradient (color, psu/100 km). The mean fields are calculated in the period from August 2011 to December 2014, with the "Microwave Optimally interpolated Sea Surface Temperature products" from Remote Sensing Systems and the IPRC/SOEST Aquarius OI-SSS v4 product. The black box indicates our study region. Latitude-depth sections of the (c) mean potential temperature and (d) mean salinity. Longitude-depth sections of the (e) mean potential temperature north and (g) south of the KE. Longitude-depth sections of the (f) mean salinity north and (h) south of the KE. The latitude-depth and longitude-depth sections are constructed by the IDW method (Yang et al., 2013) with a radius of influence of 2° for Figures 3e–3h and of 1° for Figures 3e and 3f, with all Argo float profiles outside eddies within the study region.

reveal clear signatures of L-CMW. Part of the reason might be that the formation region of L-CMW shifts southeastward (Oka et al., 2011), crossing the KE axis. North of the KE, Denser Central Mode Water (D-CMW, $\theta = 8$–10.5°C, S = 33.8–34.2 psu, $\sigma_\theta = 26.1$–26.5 kg/m^3) and TRMW are present in the upper layer, while Pacific Subarctic Water (PSW, $\theta = 2$–4°C, S = 33.5–34.5 psu) stays in the intermediate water layer below.

As to the large-scale water mass distribution, we present the cross sections of the mean potential temperature and salinity across the study region in Figure 3. The large-scale SST and SSS gradients in the study region are predominantly southward. The region south of the KE is the northern part of the SSS maximum in the subtropical North Pacific. The main thermocline extends from about 500 m south of the KE to near the sea surface north of the KE. Correspondingly, isopycnals deepen from the north to the south. In the
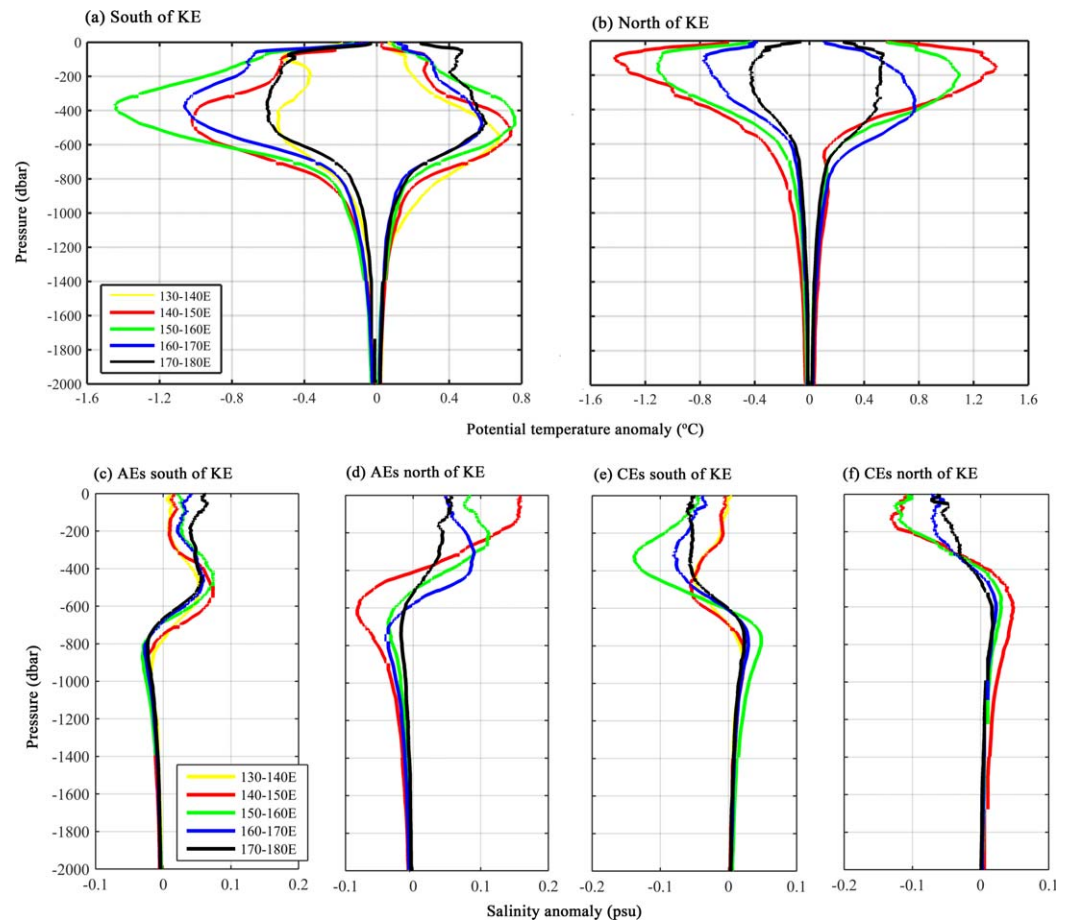
Figure 4. Mean vertical profiles of θ' for AEs and CEs in all subregions (a) south and (b) north of the KE. The lines in the right (left) of each diagram represent the anomalies for AEs (CEs). Mean vertical profiles of salinity anomaly for (c, d) AEs and (e, f) CEs (c, e) south and (d, f) north of the KE.

zonal sections south of the KE (Figures 3g and 3h), isopycnals are tilted downward from east to west, indicating a southward geostrophic flow, consistent with the Sverdrup balance. Zonal sections north of the KE (Figures 3e and 3f), corresponding to the subpolar gyre, present isopycnals tilting downward from west to east, and are also in line with the Sverdrup balance. Both the θ-S diagrams and the meridional sections show that the meridional variations of the upper ocean stratification are larger than the zonal variations. In the following, both the meridional and zonal variations of the eddy vertical structures are discussed.

Figures 4a and 4b show the mean θ' profiles for eddies in the nine subregions north and south of the KE. The eddy-induced θ' reach 1–2°C in the main thermocline, and a large discrepancy exists in the meridional direction. Eddy structures are dominated by subsurface anomalies south of the KE; while north of the KE, eddy-induced anomalies are intensified near the surface. This is consistent with the different background stratifications north and south of the KE (Figures 3c and 3d), and similar results were obtained by Amores et al. (2017a) for mesoscale eddies in the North Atlantic subtropical gyre. Largest temperature and salinity anomaly magnitudes for both AEs and CEs are found along the path of the KE jet between 140°E and 160°E. This is in agreement with results from Sasaki and Minobe (2015), who found eddies shed from the KE played a dominant role in the meridional heat transport across the KE jet, which will be further discussed below.

The gradual change in the eddy-induced temperature anomaly structure with longitude north and south of the KE is shown in Figures 5a–5d. The IDW interpolation method is applied here to a uniform 0.5° grid along longitude from 130°E to 180°E for eddy θ' profiles north and south of the KE, neglecting meridional variations on smaller scales. The radius of influence here is R = 2°. The nonparametric Mann-Whitney U test is applied to provide an indication of the statistical significance of the θ' structures (Chaigneau et al., 2011).

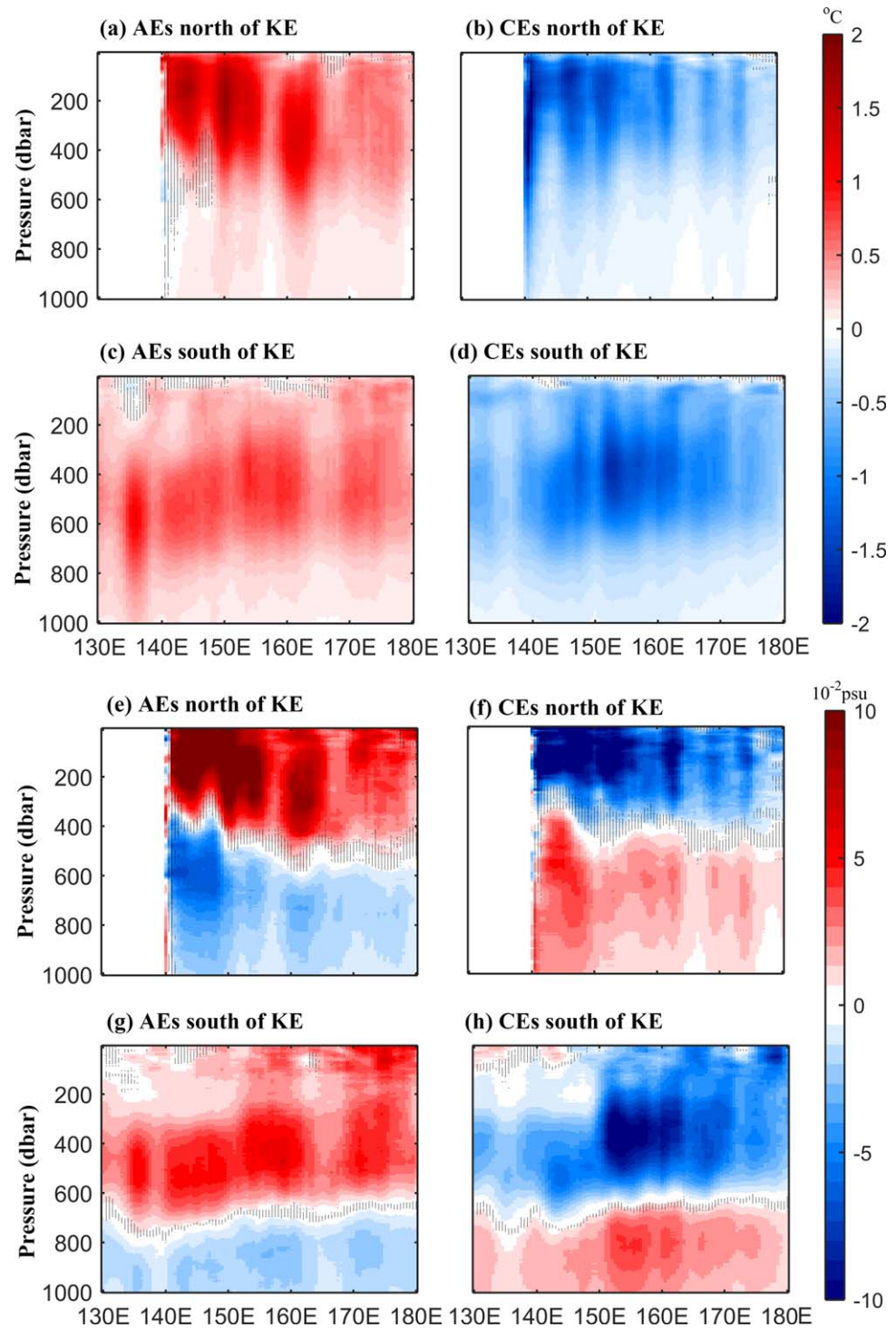**Figure 5.** θ' of (a, c) AEs and (b, d) CEs as function of longitude (a, b) north and (c, d) south of the KE. S′ of (e, g) AEs and (f, h) CEs as function of longitude (e, f) north and (g, h) south of the KE. A composite nonparametric Mann-Whitney U test shows where θ' or salinity anomalies are significantly different from 0 at the 95% confidence level (nondotted regions).

For AEs south of the KE (135°E–180°E), the westward strengthening and deepening of eddy signals is evident. Reasons might be (1) the influence of background stratification characterized by a westward deepening isopycnals and (2) the generation of more energetic eddies with more deep-reaching anomalies farther west, where the KE jet is more energetic as well. North of the KE, AEs in region F show cold and fresh signals
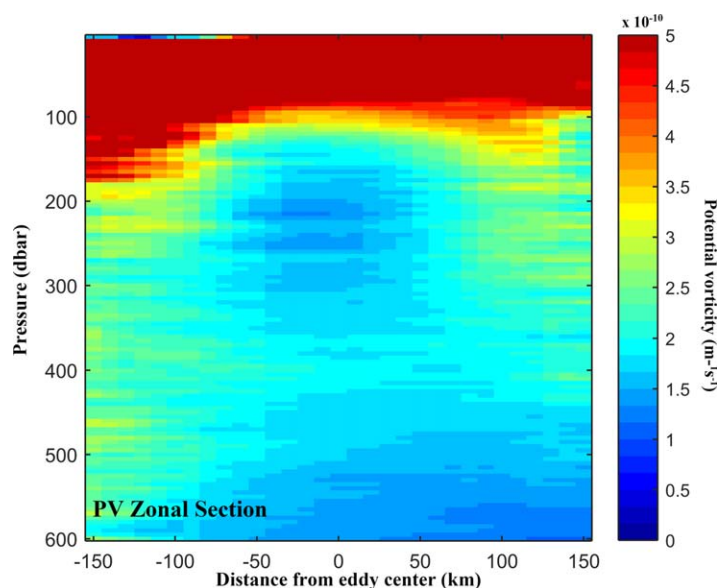
Figure 6. Zonal section of PV through the eddy center for AEs in region F (the low-PV core in the upper layer, and the low-PV values in the deeper layers are visible).

in the depth range 400–800 dbar, making the westward strengthening eddy signal (in terms of anomaly magnitude) only evident in the upper water layers. Although cold signatures are not significantly different from 0, these cold signals provide some clues for the characterization of AE types there (the cold area spans from 140°E to 145°E, and the sampling numbers there are much larger than 30). Near-surface water properties vary strongly, impacted by air-sea heat and freshwater fluxes, and near-surface mixing. Thus it is reasonable that eddy anomalies near the sea surface do not pass the U test, which is not the case in deeper layers, where other reasons may matter.

Itoh and Yasuda (2010b) reported that warm and saline AEs near Japan and the Kuril-Kamchatka Trench have a double-core structure, with a cold and fresh core below the warm core. Here the cold signals weaken toward the east and disappears near 145°E, so the cold signals in the eddy vertical profile in region F (Figure 4) are biased by the warm signals from other general warm-core AEs (the number of negative θ' is comparable to that of normal positive θ' in areas where cold signatures are found in region F). Itoh and Yasuda (2010b) proposed that this kind of double-core eddy structure is caused by the interaction of warm and cold water masses, both of which have low PV. Interestingly in region F (Figure 6), we find low-PV cores for AEs in the depth range 140–400 dbar (upper layers), and also below 500 dbar (all pass the U test). This further verifies the hypothesis from Itoh and Yasuda (2010b; PV eddy composites are also checked in regions G-I, but no low-PV core in the upper layers can be found). In addition, we can clearly see the large cold and fresh signals for AEs in region F at 600 dbar, whereas the negative θ' and S' signals for AEs in other regions are much weaker.

The vertical sections of the mean θ' of the composite AEs and CEs at different pressure levels are shown in Figure 7. Most eddy cores are shifted to the west with large anomalies in the west of or near the KE jet (except region A), suggesting poleward heat transports by mesoscale eddies (Qiu & Chen, 2005). We also found that the anomaly magnitude decreases with depth, having little impact below 1,000 dbar (Figures 4 and 8, the three-dimensional structures of θ' for AEs and CEs in region H and region C). The eddy patterns northwest of the KE are more irregular, and part of the reason may be the complex ocean conditions, such as the energetic cold Oyashio water intrusion, the warm KE meander as well as the meridional and zonal variations of the KE path.

Figures 4c–4f show the mean S' profiles in all nine subregions. The change in magnitude of S' along the longitude axis (Figures 5e–5h) is similar to the variations of θ'. AEs/CEs north of the KE have positive/negative S' in the surface layer with larger magnitude (near-surface maximum), accompanying with negative/positive values in deeper layers (maximum at about 700–800 dbar) with smaller magnitude. The eddy salinity structure as function of longitude provides similar information as the eddy temperature structure, such as the westward shift of maximum anomalies, the stronger signals of eddies shed from the KE, and the double-core eddies northwest of the KE (the fresher waters from 400 to 800 dbar in region F suggests the origin in the Oyashio). The vertical sections of the mean S' composites for AEs and CEs at the same pressures as the θ' sections are shown in Figure 9. The westward shift of S' cores are also presented, with larger amplitudes in the west or near the KE (except region A), suggesting poleward eddy-induced salt transports (Qiu & Chen, 2005).

3.2. Eddy Heat and Salt Transport
3.2.1. Comparison With MZ Method and CH12 Data Set
To validate our results, we modified the method by Zhang et al. (2014; MZ method, see Appendix D for details), which is originally applied to derive eddy mass transports, to recalculate the heat transport by eddy movements. The meridional eddy heat transports calculated from our method and MZ method in the KE region are compared in Figures 10a and 10b. The trends and values of the total meridional eddy heat transports are consistent for both methods. The total meridional eddy heat transport values are smaller in
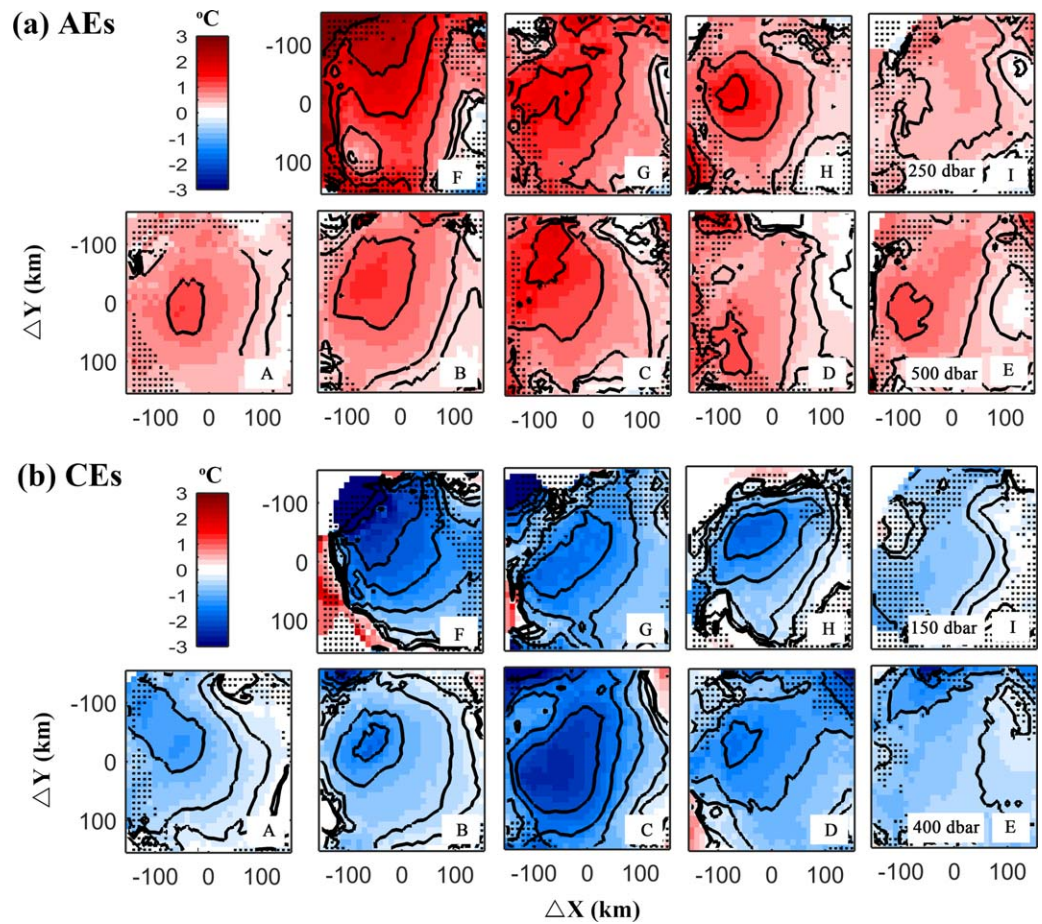
Figure 7. Eddy temperature anomaly composites for (a) AEs at 500 dbar in regions A–E, and at 250 dbar in regions F–I; (b) CEs at 400 dbar in regions A–E, and at 150 dbar in regions F–I. Nondotted areas indicate where composite temperature anomalies are significantly different from 0 at the 95% confidence level.

magnitude in regions 25°N–30°N and 40°N–45°N than the region near the KE jet, suggesting that eddies shed off the KE are the main contributors to the poleward eddy heat transport. The meridional heat transport of CEs is larger than that of AEs over the vicinity of the KE. The magnitude of eddy-induced meridional
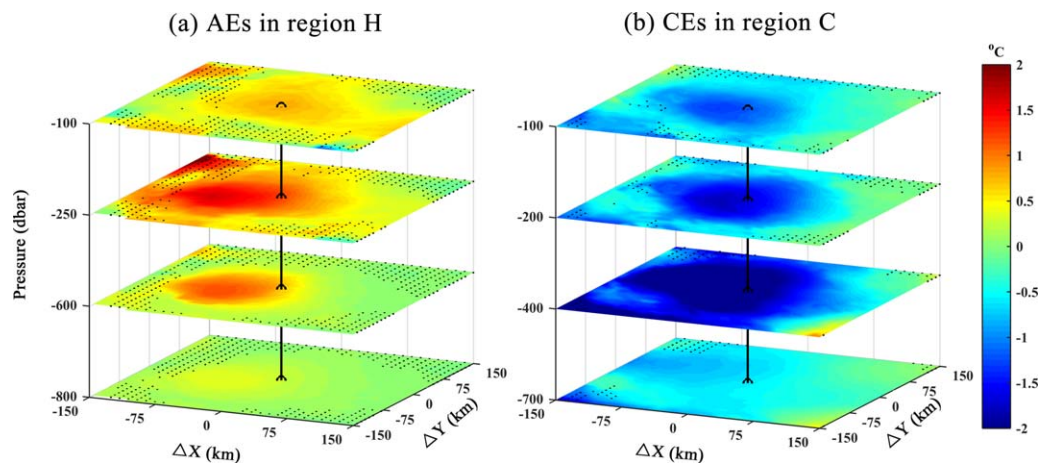
Figure 8. The 3-D structures of θ' for (a) AEs in region H and (b) CEs in region C. The black line marks the eddy center. Nondotted areas indicate where composite temperature anomalies are significantly different from 0 at the 95% confidence level.
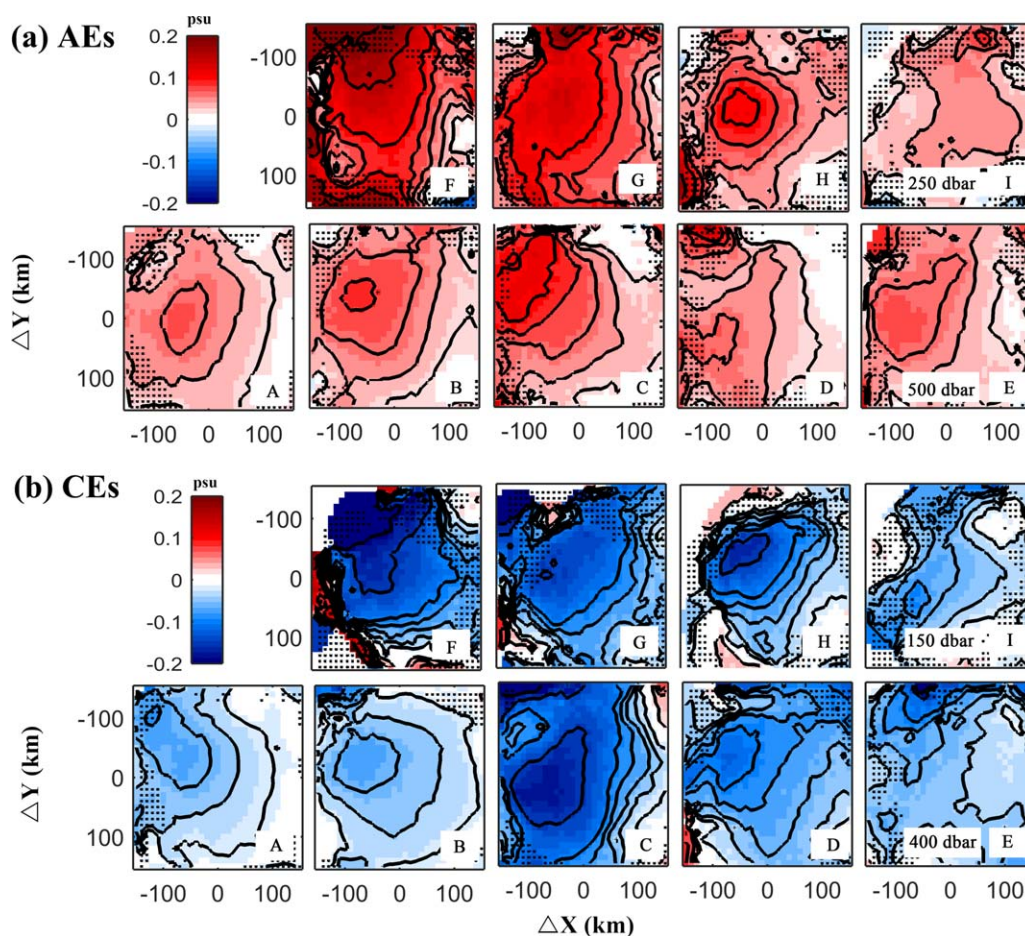
Figure 9. Eddy salinity anomaly composites for (a) AEs at 500 dbar in regions A–E, and at 200 dbar in regions F–I; (b) CEs at 400 dbar in regions A–E, and at 150 dbar in regions F–I. Nondotted areas indicate where composite temperature anomalies are significantly different from 0 at the 95% confidence level.

heat transport is on the order of 0.01 PW. These estimated values represent a lower bound of eddy-induced heat transport, considering that weaker eddies may be ignored due to the applied amplitude threshold or the smoothed SLA data from the CMEMS (Castelao, 2014; Chelton et al., 2011). It should be noted that eddy heat and salt transports from Dong et al. (2014) are bin-size dependent, they consider the eddy-trapping effect as a block shape instead of a circular shape from our method. Given these concerns, it is not appropriate to make a direct comparison between their and our results for either eddy heat or salt transport. Instead, we compare the results from our method with those from the MZ method (Figures 10a and 10b) to test the robustness of the estimates.

It is also interesting to compare the eddy heat transports in the KE region as obtained from different eddy data sets. Having been widely used in various studies, the CH12 data are applied here with our method. As shown in Figures 10c and 10d, the magnitudes of eddy-induced heat transports are consistent in both data sets: again on the order of 0.01 PW. However, the zonal heat transports from CH17 is generally smoother than the one derived from CH12 (Figure 10d). One possible explanation could be that the CH12 data are derived from weekly SLA data, and the tracked eddy paths are not as continuous as those derived from the daily SLA data, which suggests that the results from CH12 data may contain more sampling errors compared with those from CH17 data. In Figure 10c, two peaks and one valley of the eddy-induced meridional heat transports can be found for both AEs and CEs near the KE jet (35°N) from both CH17 and CH12 data. The KE jet sheds off eddies north and south of its boundaries, so the southern peak of CEs and northern peak of AEs (Figure 10c) may mainly represent eddies from the KE jet. Both the trends and magnitudes of the eddy heat transports are consistent between the CH12 and CH17 data, and the detailed discrepancies
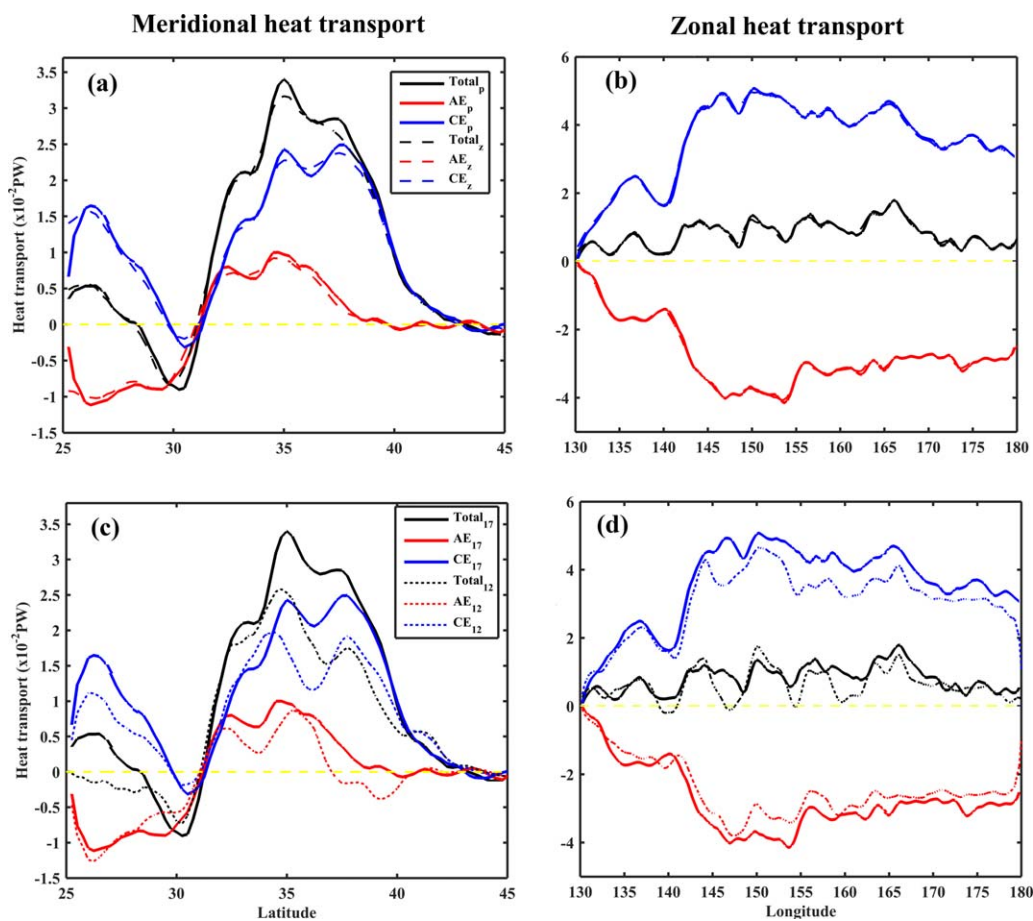
Figure 10. (a, c) The zonally integrated meridional heat transport by mesoscale eddies in the Northwestern Pacific Ocean (130°E–180°E, except the Sea of Japan). (b, d) The meridionally integrated zonal heat transport by mesoscale eddies in the Northwestern Pacific Ocean (25°N–45°N, except the Sea of Japan). In Figures 10a and 10b, z represents the results from MZ method (dashed lines); p represents results from our method (solid lines), they are calculated based on the CH17 data. In Figures 10c and 10d, 17 represent the results based on CH17 data (solid lines); 12 represents the results based on CH12 data (dotted lines), they are calculated with our method. Red, blue, and black lines represent the heat transports by AEs, CEs, and all eddies, respectively.

may result from differences in eddy detection methods, data processing, etc. Understanding these differences is beyond the scope of this study.

3.2.2. Spatial Distributions of Heat and Salt Transports by Eddy Movements

Figure 11a shows the distribution of meridional eddy heat transport in the Northwestern Pacific Ocean from our method based on CH17 data. The zonal heat transport by eddy movements across our study region (25°N–45°N, except the Sea of Japan) is shown in Figure 10b, and the distribution map is shown in Figure 11b. The patterns of eddy heat transport are closely associated with eddy distributions and movements. Itoh and Yasuda (2010a) pointed out that eddies in the KOER are intensively distributed near topography and quasi-stationary hydrographic features (supporting information Figure S-1); both AEs and CEs propagate poleward along the trenches, while the long-distance westward movements of eddies are also obvious east of the KE. For AEs (CEs), broad westward (eastward) heat transport is evident both south and north of the KE, as most eddies propagate westward. In accordance with results of Zhang et al. (2014) that focus on eddy mass transport, large westward eddy heat transport is found in the latitude band 25°N–40°N. Exceptions are along the path of the Kuroshio and the KE, where eddies are advected by the energetic currents, resulting in northward and eastward heat transport for AEs, respectively. Also, eddy movements along the Kuril-Kamchatka Trench and the Subarctic Front northeastward results in different eddy heat transport directions compared to the surroundings. The meridionally integrated eddy zonal heat transport for AEs and CEs largely compensates each other, resulting in a weak total zonal heat transport (Figure 10b).
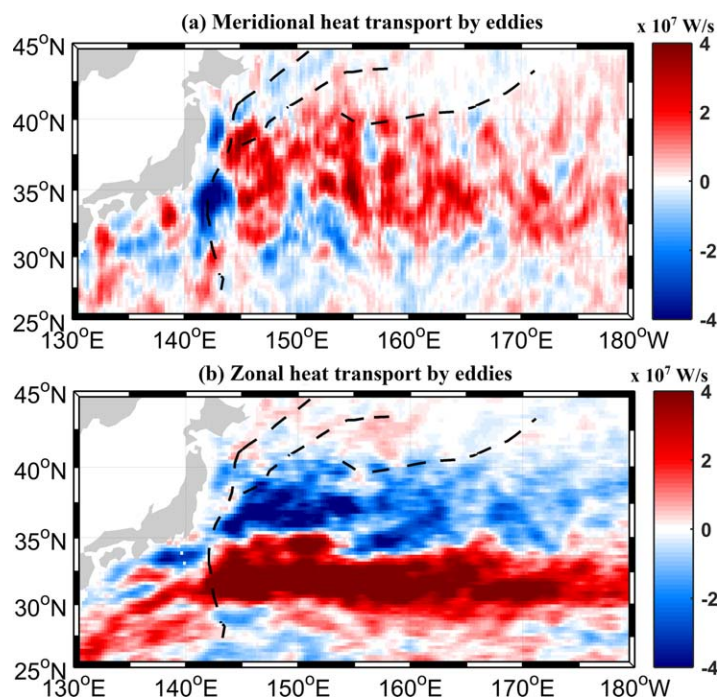
Figure 11. The (a) meridional and (b) zonal heat transport by eddies from our method (based on CH17 data). The JT, the KKT, the SAF, and the SAB are shown by black dashed lines (cf., Figure 1).

The salt transport by eddy movements is presented in Figure 12, expressed in terms of an equivalent freshwater volume flux. The patterns of the eddy freshwater transport resemble that of the heat transport. The overall magnitude is on the order of 10^3 m^3/s. Eddies near the KE jet (latitude bands in 30°N–40°N) contribute to a southward freshwater transport. The zonal transport is larger in longitude bands 150°E–170°E due to larger salinity anomalies trapped within eddies near the KE jet.

To estimate the large-scale impact of heat transports by eddy movements in our study region, we calculate the divergence of eddy heat transports Div_h and smooth it using a generic two-dimensional Loess filter with half width of 10° longitude and 5° latitude (Figure 13a). Here we neglect changes of the trapped heat during eddy lifetime, and only use an average eddy heat anomaly value to calculate heat transport by eddy movements. Thus, Div_h is solely generated by eddy birth and death, as well as spatial variations of mean eddy structures along eddy paths. Positive values of Div_h represent oceanic heat loss, which means heat is transported away by eddies. Large positive patches south of the KE (Figure 13a) illustrate that the ocean there loses heat due to eddy movements, more specifically, due to the relative dominance of AE births over AE deaths together with the relative dominance of CE deaths over CE births. According to the annual mean net surface heat flux (Figure 1b), the ocean near the KE jet also loses heat to the atmosphere. Interestingly, large negative patches north of the KE show that the ocean there gains heat from the eddy movements, which suggests that eddies compensate the ocean heat loss to the atmosphere. In this way, eddies contribute to the poleward heat transport from the south to the north across the KE jet.

To compare eddies' role in the heat budget with the atmospheric surface heat fluxes, we compute the ratio between the total eddy heat divergence and the annual mean net surface heat flux (Figure 13b). Regions where the absolute value of the surface heat flux is smaller than 20 W/m^2 are masked (gray patches in Figure 13b), in order to avoid large fluctuations of positive and negative ratios. In addition, we delineate the region with a net surface heat loss of more than 85 W/m^2 (inside the black dashed lines, region N) for further analysis. The physical meaning of the ratio depends on the sign of the air-sea flux. If the ocean loses heat to the atmosphere (negative sea-air flux, like region N), a negative ratio (means positive eddy heat divergence) represents the ocean loses heat (reinforcement of surface heat flux) due to eddies; whereas a positive ratio (means negative eddy heat divergence) represents the ocean gains heat (counteracting surface heat flux) due to eddies. Inside region N, the contribution of eddies constitute 27.9% of the total heat loss, whereas the maximum and minimum ratio values are 119.7% and −75.9%, respectively. Positive and negative ratios exist north and south of the KE, respectively. The percentage of pixels with a negative (positive) ratio in region N is 72.2% (26.8%). The average heat losses due to the eddy heat divergence in regions with negative and positive ratios within region N are 33.3 and −29.7 W/m^2, respectively, resulting in a total average heat loss due to the eddy heat transport divergence in region N of 12.6 W/m^2 (SD = 15.0 W/m^2).

4. Summary and Discussion

Based on satellite altimetry data and Argo float profiles, three-dimensional eddy structures, heat and salt transports by eddy movements in the Northwestern Pacific Ocean (25°N–45°N, 130°E–180°W) are investigated. Eddies dominantly show subsurface (near-surface) θ/S anomalies south (north) of the KE. A general westward strengthening and deepening of eddy anomalies are clearly observed, but with exceptions in regions A and F. In region F, cold signals are found for AEs in deeper layers (400–800 dbar), which might be due to eddies generated from the interaction of warm-core eddies with low PV from the KE jet and the low-PV cold-core AEs from the north. In region A, cold signals are found for AEs in the upper 100 dbar. These
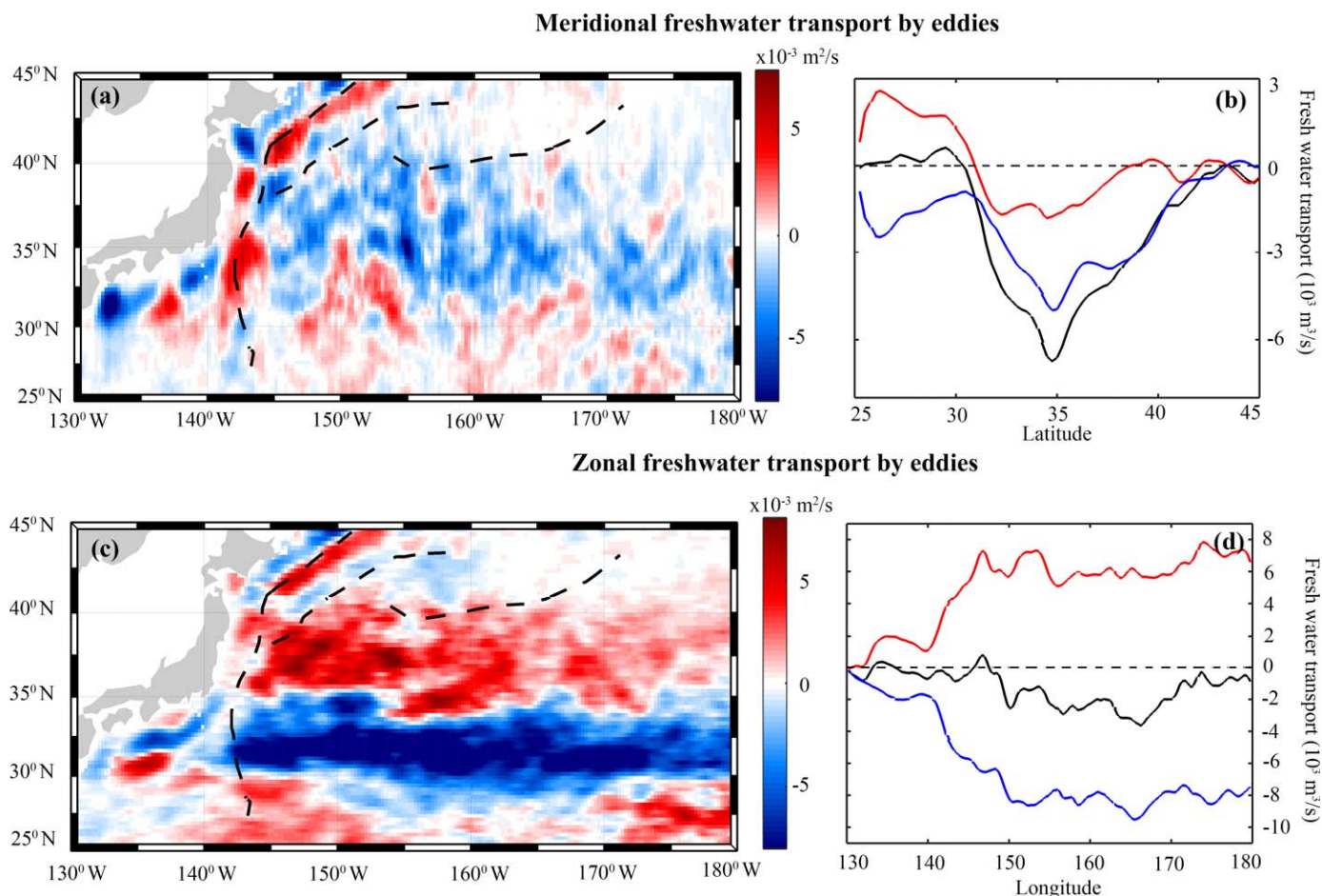
Figure 12. The (a) meridional and (c) zonal freshwater transport by eddies from our method (based on CH17 data). The JT, the KKT, the SAF, and the SAB are delineated by black dashed lines (cf., Figure 1). (b) The zonally integrated meridional freshwater transport by mesoscale eddies in the Northwestern Pacific Ocean (130°E–180°E, except the Sea of Japan). (d) The meridionally integrated zonal freshwater transport by mesoscale eddies in the Northwestern Pacific Ocean (25°N–45°N, except the Sea of Japan). Red, blue, and black lines in Figures 12b and 12d represent the heat transports by AE, CE, and all eddies, respectively.

types of eddies have been reported by Hosoda and Hanawa (2004), and understanding their possible origin and impact is beyond the scope of the present study.

Sun et al. (2017) recently showed climatological eddy composites within our study region (with a horizontal resolution of 0.25°) for AEs and CEs. They pointed out that the maximum cold (warm) anomaly in the composite CE (AE) is −2°C at 360 m (1.78°C at 410 m); and the maximum salinity anomaly is −0.13 psu at 260 m and 0.12 psu at 260 m for CE and AE composites, respectively. These values are within the range of our estimates, but overall smaller than ours (Figures 7 and 9). For example, the largest salinity anomaly for AEs in region F at 250 dbar reaches 0.3 psu, and 29% of the anomalies are larger than 0.12 psu. These discrepancies may be largely due to different data and processing procedures. First, Sun et al. (2017) defined one eddy analysis area (4.25° × 4.25°) around the eddy center, and collected all Argo float profiles within this region with a time window of one week (weekly SLA data are used) for calculation; whereas we use eddy boundaries to determine whether Argo floats are inside eddies, and our time window for collecting Argo floats is 1 day. Second, they only computed one AE and one CE eddy composites in the region 140°E–180°E, 28°N–40°N, which smeared out spatial variations. For example, the magnitudes of eddy anomalies near the western part of the KE (Figures 7 and 9) are much larger than those east of the KE. The methods of Sun et al. (2017) ensured large sampling number and reliability for calculating the climatological eddy composites, but their composites tend to be more symmetrically smoothed and weakened as Argo float profiles outside eddies were likely included in the averaging. Furthermore, one recent study from Amores et al. (2017b) proposes that an eddy of given polarity tends to be surrounded by eddies of opposite polarity,
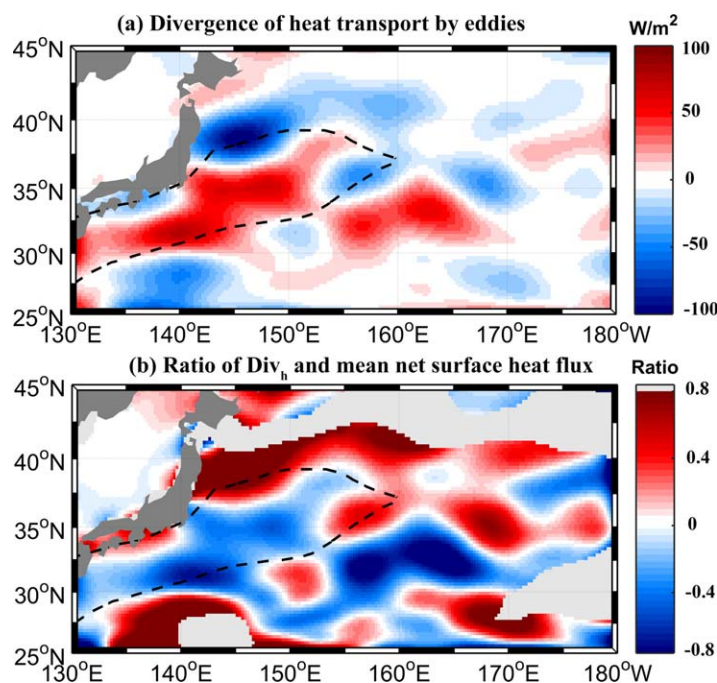
Figure 13. (a) Divergence of the heat transport by eddies from our method. (b) Ratio between the eddy heat transport divergence shown in Figure 13a and the annual mean net surface heat flux. Regions where the magnitudes of the annual mean net surface heat flux are smaller than 20 W/m^2 are masked (gray patches). Black dashed contours delineate the region losing heat by more than 85 W/m^2. Negative ratio south (north) of the gray patch near 40° N means the ocean loses (gains) heat due to eddies (because mean net surface heat flux is positive/negative in the north/south of the gray patch near 40°N).

which causes a reduction of about 20% of the eddy composite amplitude. We suppose the nonrandom distribution of eddy polarity around a given eddy may modify the eddy temperature and salinity composites calculated by Sun et al. (2017) with an eddy analysis area (4.25° × 4.25°) around the eddy center. On the other hand, our results are less impacted by other surrounding eddies, because we collect Argo profiles based on eddy boundaries, excluding profiles outside eddies. To some extent, our results can supplement their findings, and show further detailed spatial variations of eddy structures over the vicinity of the KE.

A new method, which combines the existing eddy trajectories with Argo float based three-dimensional eddy temperature and salinity information, is applied to estimate heat and salt transports by eddy movements. Its results are compared with the MZ method, which is originally formulated to calculate eddy mass transport (Zhang et al., 2014). Both methods show consistent values of the order of 0.01 PW for the meridional eddy heat transport, and 10^3 m^3/s for the meridional eddy freshwater transport. The obtained meridional eddy heat transport is smaller than values from Qiu and Chen (2005). Interestingly, in agreement with the results from Qiu and Chen (2005), the meridional heat transport along the path of the KE jet changes in directions with southward heat transport at about 142°E and 150°E with northward heat transport in between and east of 150°E (cf., Qiu & Chen, 2005, Figure 13; Figure 11a), instead of a broad northward transport reported by Stammer (1998). Southward heat transport at about 150°E, 35°N and northward heat transport east of that longitude was also observed by Wunsch (1999) with moored current meters in the KE region. Qiu and Chen (2005) estimated the eddy meridional heat transport using the equation $\langle \rho c_p T' v' \bar{D}_e \rangle$, where v' is calculated geostrophic velocity from SLA data, T' is the zonally high-pass filtered (with a zonal cutoff scale of 10°) TMI SST, D_e is defined as an effective depth which converts the surface eddy heat transport to a depth-integrated value. D_e is 177 m in the subtropical Pacific Ocean as calculated with 102 Argo floats. We compare the estimated meridional eddy heat transports between these studies: near the upstream of the KE (130°E–160°E), our value is of smaller magnitude than that of Qiu and Chen (2005) by about 10%–40%; in the region 160°E–180°E, both results are more comparable. Part of the reason for this difference may be that we only use coherent eddies, which are automatically detected and trackable for more than one month; whereas Qiu and Chen (2005) treated the entire mesoscale variability with zonal scales smaller than 10° as eddies. So meanders, which are common and often stationary near the KE, and other mesoscale structures were included in their estimation but neglected in our calculation, which likely caused their estimates larger than ours. As to the meridional heat transport patterns, the detailed spatially alternating eddy heat transport distributions over the vicinity of the KE in our method also show differences compared with theirs. For example, the transport near the Japan Trench is positive in Qiu and Chen (2005) but shows negative values in our study. One main reason is that our results are directly associated with the heat transport due to eddy movements. CEs dominate in this region (Itoh & Yasuda, 2010a), their movements to the north contribute more to the meridional heat transport, resulting in a southward eddy heat transport. Also in their method, meanders south of Japan might play a dominant role in eddy heat transport. Likewise, the eddy heat transport near the coastlines in their method may include the impact of meanders (large positive patches in the north), while ours completely neglect their influences. The different definitions of eddies above also apply to the discrepancies between our Lagrangian method and all methods in an Eulerian framework.

For the first time, we present detailed spatial distribution of salt and heat transports by eddy movements in the Northwestern Pacific Ocean. It should be noted that only mesoscale eddies detected by satellite and recorded by CH17 data set have been included for the calculation of eddy transports, so submesoscale eddies, subsurface-intensified eddies or other weak mesoscale eddies which are not easily captured by

satellite altimeter are neglected here. Furthermore, we calculate the divergence of eddy heat transport, with which we can consider the impacts of both eddy death and eddy birth. Large patches of positive eddy heat transport divergence south of the KE jet suggest that the ocean (the Kuroshio and the KE) there provides heat to both eddies and atmosphere; whereas north of the KE jet, eddies partly compensate the ocean heat loss to the atmosphere.

We computed the ratio between the total eddy heat transport divergence and the annual mean net surface heat flux, and proposed the important role of ocean eddies in the upper ocean heat budget compared to surface heat fluxes. The negative/positive divergence of the eddy heat transport north/south of the KE indicates a northward eddy heat transport across the KE jet. It should be noted that mesoscale eddies can locally impact surface turbulent heat fluxes, including turbulent latent and sensible heat fluxes (Ma et al., 2016; Villas Bôas, et al., 2015). But our goal is to study the large-scale impact of eddy heat transports, so the eddy heat transport divergence map is smoothed using a filter with half width of 10° longitude and 5° latitude, and the spatial resolution of the atmospheric net heat flux is 2.5°. By doing so, we neglected the impacts of mesoscale air-sea interactions to the upper ocean heat budget, because warm and cold eddy-induced turbulent heat fluxes tend to cancel each other by averaging over a large area.

These results may be useful for the validation of high-resolution climate models. Once validated, realistic models can be further used to address questions such as: What are the generation mechanisms of AEs south of the KE? How are eddies with negative temperature anomalies near the Shikoku Recirculation Gyre generated? These questions are difficult to solve by observational analyses alone. Moreover, when applying our Lagrangian based heat flux method to an eddy-resolving ocean model simulation where sampling is less of an issue, one can further test the accuracy of the Lagrangian method compared to other conventional approaches. As eddies and their interaction with the atmosphere contribute to shape the Kuroshio, its extension, and the related poleward heat transport (Ma et al., 2016), dynamics and impact of ocean eddies deserves further investigation.

Appendix A: Argo Data Preprocessing

Following Chaigneau et al. (2011) and Yang et al. (2013), we only use profiles satisfying: (1) the quality flag is 1; (2) the shallowest data are between the sea surface and 10 m depth, and the deepest is below 1,000 m; (3) at least 30 valid values are in the upper 1,000 m of each profile; (4) the property values should be in the valid range (temperature 35 to −2℃, salinity 38–30 psu); and (5) the pressure profile should monotonically increase. All profiles that passed the criterions above were linearly interpolated in the pressure range 0–2,000 dbar with 5 dbar as the vertical resolution (constant extrapolation toward the surface).

Appendix B: CH17 and CH12 Eddy Data Set

The CH17 eddy data set is the newest and its previous versions (such as CH12 eddy data set) have been applied widely, we use it as a reference data set, especially for eddy trajectories. Besides the newest daily SLA data set, their eddy identification and tracking procedure were also modified substantially, see Schlax and Chelton (2016) for details. Instead of defining eddies by an outermost closed contour of SLA, each eddy was defined on basis of connected pixels that satisfy specified criteria. As to the CH12 eddy data set, refer to Chelton et al. (2011) for more details.

Appendix C: FAG Eddy Detection Method

FAG method first searches for the local extrema over a 5 × 5 neighborhood (unit: pixel) in the SLA field (maximum and minimum for AEs and CEs, respectively), then calculate possible eddy boundaries around each extremum. The eddy area is obtained by iteratively thresholding around the extrema and binarization depending on whether the SLA at the grid points exceeds a certain threshold. The threshold starts from the value at the extremum, and is automatically increased (decreased) by 0.5 cm (eddy amplitude is defined as the difference between the extremum and the average SLA along the eddy boundary, and the smallest eddy amplitude is 1 cm). When the threshold increases (decreases), the eddy contour grows until another extremum is contained inside. Then the contour is set to be the one when the threshold at the last step is applied and only one extremum should be within the eddy boundary.

Appendix D: MZ Method for Eddy Transport Calculation and Validation

As Zhang et al. (2014) only calculated oceanic mass transport by mesoscale eddy movements, we replace the eddy volume with the calculated eddy heat and salt anomaly in their equations to calculate the eddy heat and salt transports in the Northwestern Pacific Ocean. Because we modified their method for wide applications, we call it the MZ method in this paper. Here we simply introduce the calculation details. The heat anomaly H_{ea} and propagation velocity (C_x and C_y are zonal and meridional eddy propagation velocities, respectively) for each eddy are calculated using the same approach as our method with eddy trajectories. To calculate the distribution of eddy-induced heat transports, we lay out a uniform $0.25° \times 0.25°$ grid in our study region, and set up an average box of $1.25°$ meridional length (D_{lat}) and a $1.25°$ zonal length (D_{lon}) around each grid point. For each detected eddy, the zonal heat transport by this eddy is $H_{ea} \cdot C_x$. For each grid point, sum all eddy-induced transports within the average box for the whole period from January 1993 to December 2014, and divide it by the number of snapshots (here the number of days N for daily SLA data), the zonal length D_{lon} and the meridional length D_{lat}, the average eddy-induced zonal heat transport (unit: W/m) is

$$Q_x = \frac{\sum H_{ae} \cdot C_x}{D_{lat} \cdot D_{lon} \cdot N}$$

Similarly, we can compute the eddy-induced meridional heat transport Q_y within the same average box:

$$Q_y = \frac{\sum H_{ae} \cdot C_y}{D_{lat} \cdot D_{lon} \cdot N}$$

References

Amores, A., Melnichenko, O., & Maximenko, N. (2017a). Coherent mesoscale eddies in the North Atlantic subtropical gyre: 3-D structure and transport with application to the salinity maximum. *Journal of Geophysical Research: Oceans*, *122*, 23–41. https://doi.org/10.1002/2016JC012256

Amores, A., Monserrat, S., Melnichenko, O., & Maximenko, N. (2017b). On the shape of sea level anomaly signal on periphery of mesoscale ocean eddies. *Geophysical Research Letters*, *44*, 6926–6932. https://doi.org/10.1002/2017GL073978

Castelao, R. M. (2014). Mesoscale eddies in the South Atlantic Bight and the Gulf Stream Recirculation region: Vertical structure. *Journal of Geophysical Research: Oceans*, *119*, 2048–2065. https://doi.org/10.1002/2014JC009796

Chaigneau, A., Le Texier, M., Eldin, G., Grados, C., & Pizarro, O. (2011). Vertical structure of mesoscale eddies in the eastern South Pacific Ocean: A composite analysis from altimetry and Argo profiling floats. *Journal of Geophysical Research*, *116*, C11025. https://doi.org/10.1029/2011JC007134

Chelton, D. B., Deszoeke, R. A., Schlax, M. G., El Naggar, K., & Siwertz, N. (1998). Geographical variability of the first baroclinic Rossby radius of deformation. *Journal of Physical Oceanography*, *28*(3), 433–460.

Chelton, D. B., Schlax, M. G., & Samelson, R. M. (2011). Global observations of nonlinear mesoscale eddies. *Progress in Oceanography*, *91*(2), 167–216. https://doi.org/10.1016/j.pocean.2011.01.002

Chelton, D. B., Schlax, M. G., Samelson, R. M., & de Szoeke, R. A. (2007). Global observations of large oceanic eddies. *Geophysical Research Letters*, *34*, L15606. https://doi.org/10.1029/2007GL030812

Dong, C., McWilliams, J. C., Liu, Y., & Chen, D. (2014). Global heat and salt transports by eddy movement. *Nature Communications*, *5*, 3294. https://doi.org/10.1038/ncomms4294

Ebuchi, N., & Hanawa, K. (2000). Mesoscale eddies observed by TOLEX-ADCP and TOPEX/POSEIDON altimeter in the Kuroshio recirculation region south of Japan. *Journal of Oceanography*, *56*(1), 43–57. https://doi.org/10.1023/A:1011110507628

Ebuchi, N., & Hanawa, K. (2001). Trajectory of mesoscale eddies in the Kuroshio recirculation region. *Journal of Oceanography*, *57*, 471–480.

Faghmous, J. H., Frenger, I., Yao, Y., Warmka, R., Lindell, A., & Kumar, V. (2015). A daily global mesoscale ocean eddy dataset from satellite altimetry. *Scientific Data*, *2*, 150028.

Flierl, G. R. (1981). Particle motions in large-amplitude wave fields. *Geophysical & Astrophysical Fluid Dynamics*, *18*, 39–74.

Hosoda, K., & Hanawa, K. (2004). Anticyclonic eddy revealing low sea surface temperature in the sea south of Japan: Case study of the eddy observed in 1999–2000. *Journal of Oceanography*, *60*(4), 663–671. https://doi.org/10.1007/s10872-004-5759-9

Isoguchi, O., Kawamura, H., & Oka, E. (2006). Quasi-stationary jets transporting surface warm waters across the transition zone between the subtropical and the subarctic gyres in the North Pacific. *Journal of Geophysical Research*, *111*, C10003. https://doi.org/10.1029/2005JC003402

Itoh, S., & Sugimoto, T. (2001). Numerical experiments on the movement of a warm-core ring with the bottom slope of a western boundary. *Journal of Geophysical Research*, *106*(C11), 26851–26851. https://doi.org/10.1029/2001JC000789

Itoh, S., & Yasuda, I. (2010a). Characteristics of mesoscale eddies in the Kuroshio–Oyashio extension region detected from the distribution of the sea surface height anomaly. *Journal of Physical Oceanography*, *40*(5), 1018–1034. https://doi.org/10.1175/2009JPO4265.1

Itoh, S., & Yasuda, I. (2010b). Water mass structure of warm and cold anticyclonic eddies in the Western Boundary Region of the Subarctic North Pacific. *Journal of Physical Oceanography*, *40*(12), 2624–2642. https://doi.org/10.1175/2010JPO4475.1

Itoh, S., Yasuda, I., Ueno, H., Suga, T., & Kakehi, S. (2014). Regeneration of a warm anticyclonic ring by cold water masses within the western subarctic gyre of the North Pacific. *Journal of Oceanography*, *70*(3), 211–223. https://doi.org/10.1007/s10872-014-0225-9

Kalnay, E., Kanamitsu, M., Kistler, R., Collins, W., Deaven, D., Gandin, L., . . . Joseph, D. (1996). The NCEP/NCAR 40-year reanalysis project. *Bulletin of the American Meteorological Society*, *77*, 437–470.

Kouketsu, S., Kaneko, H., Okunishi, T., Sasaoka, K., Itoh, S., Inoue, R., & Ueno, H. (2016). Mesoscale eddy effects on temporal variability of surface chlorophyll a in the Kuroshio Extension. *Journal of Oceanography*, *72*(3), 439–451. https://doi.org/10.1007/s10872-015-0286-4

Kouketsu, S., Tomita, H., Oka, E., Hosoda, S., Kobayashi, T., & Sato, K. (2012). The role of meso-scale eddies in mixed layer deepening and mode water formation in the western North Pacific. *Journal of Oceanography*, *68*(1), 63–77. https://doi.org/10.1007/s10872-011-0049-9

Kusakabe, M., Andreev, A., Lobanov, V., Zhabin, I., Kumamoto, Y., & Murata, A. (2002). Effects of the anticyclonic eddies on water masses, chemical parameters and chlorophyll distributions in the Oyashio current region. *Journal of Oceanography*, *58*(5), 691–701.

Ma, J., Xu, H., Dong, C., Lin, P., & Liu, Y. (2015a). Atmospheric responses to oceanic eddies in the Kuroshio Extension region. *Journal of Geophysical Research: Atmosphere*, *120*, 6313–6330. https://doi.org/10.1002/2014JD022930

Ma, X., Chang, P., Saravanan, R., Montuoro, R., Hsieh, J.-S., Wu, D., . . . Jing, Z. (2015b). Distant influence of Kuroshio eddies on North Pacific weather patterns? *Scientific Reports*, *5*, 17785.

Ma, X., Jing, Z., Chang, P., Liu, X., Montuoro, R., Small, R. J., . . .Wu, L. (2016). Western boundary currents regulated by interaction between ocean eddies and the atmosphere. *Nature*, *535*(7613), 533–537. https://doi.org/10.1038/nature18640

Miyazawa, Y., Guo, X., & Yamagata, T. (2004). Roles of mesoscale eddies in the Kuroshio paths. *Journal of Physical Oceanography*, *34*(10), 2203–2222.

Nagano, A., Ichikawa, K., Ichikawa, H., Konda, M., & Murakami, K. (2013). Volume transports proceeding to the Kuroshio Extension region and recirculating in the Shikoku Basin. *Journal of Oceanography*, *69*(3), 285–293. https://doi.org/10.1007/s10872-013-0173-9

Oka, E., Kouketsu, S., Toyama, K., Uehara, K., Kobayashi, T., Hosoda, S., & Suga, T. (2011). Formation and subduction of central mode water based on profiling float data, 2003–08. *Journal of Physical Oceanography*, *41*(1), 113–129. https://doi.org/10.1175/2010JPO4419.1

Pegliasco, C., Chaigneau, A., & Morrow, R. (2015). Main eddy vertical structures observed in the four major Eastern Boundary Upwelling Systems. *Journal of Geophysical Research: Oceans*, *120*, 6008–6033. https://doi.org/10.1002/2015JC010950

Qiu, B., & Chen, S. (2005). Eddy-induced heat transport in the subtropical North Pacific from Argo, TMI, and altimetry measurements. *Journal of Physical Oceanography*, *35*(4), 458–473.

Roemmich, D., & Gilson, J. (2001). Eddy transport of heat and thermocline waters in the North Pacific: A key to interannual/decadal climate variability? *Journal of Physical Oceanography*, *31*(3), 675–687.

Saitoh, S., Inagake, D., & Sasaoka, K. (1998). Satellite and ship observations of Kuroshio warm-core ring 93A off Sanriku, Northwestern North Pacific, in spring. *Journal of Oceanography*, *54*(1997), 495–508. https://doi.org/10.1007/BF02742451

Sasaki, Y. N., & Minobe, S. (2015). Climatological mean features and interannual to decadal variability of ring formations in the Kuroshio Extension region. *Journal of Oceanography*, *71*(5), 499–509.

Schlax, M. G., & Chelton, D. B. (2016). *The "growing method" of eddy identification and tracking in two and three dimensions*. Corvallis, OR: College of Earth, Ocean and Atmospheric Sciences, Oregon State University.

Schütte, F., Brandt, P., & Karstensen, J. (2016). Occurrence and characteristics of mesoscale eddies in the tropical northeast Atlantic Ocean. *Ocean Science*, *12*(3), 663–685.

Stammer, D. (1998). On eddy characteristics, eddy transports, and mean flow properties. *Journal of Physical Oceanography*, *28*(4), 727–739.

Sun, W., Dong, C., Wang, R., Liu, Y., & Yu, K. (2017). Vertical structure anomalies of oceanic eddies in the Kuroshio Extension region. *Journal of Geophysical Research: Oceans*, *122*, 1476–1496. https://doi.org/10.1002/2016JC012226

Tsujino, H., Usui, N., & Nakano, H. (2006). Dynamics of Kuroshio path variations in a high-resolution general circulation model. *Journal of Geophysical Research*, *111*, C11001. https://doi.org/10.1029/2005JC003118

Villas Bôas, A. B., Sato, O. T., Chaigneau, A., & Castelão, G. P. (2015). The signature of mesoscale eddies on the air-sea turbulent heat fluxes in the South Atlantic Ocean. *Geophysical Research Letters*, *42*, 1856–1862. https://doi.org/10.1002/2015GL063105

Waseda, T. (2003). On the eddy-Kuroshio interaction: Meander formation process. *Journal of Geophysical Research*, *108*(C7), 3220. https://doi.org/10.1029/2002JC001583

Waterman, S., Hogg, N. G., & Jayne, S. R. (2011). Eddy-mean flow interaction in the Kuroshio Extension region. *Journal of Physical Oceanography*, *41*(6), 1182–1208.

Wunsch, C. (1999). Where do ocean eddy heat fluxes matter? *Journal of Geophysical Research*, *104*(C6), 13235–13249.

Yang, G., Wang, F., Li, Y., & Lin, P. (2013). Mesoscale eddies in the northwestern subtropical Pacific Ocean: Statistical characteristics and three-dimensional structures. *Journal of Geophysical Research: Oceans*, *118*, 1906–1925. https://doi.org/10.1002/jgrc.20164

Yasuda, I., Ito, S.-I., Shimizu, Y., Ichikawa, K., Ueda, K.-I., Honma, T., . . . Koizumi, K. (2000). Cold-core anticyclonic eddies south of the Bussol' Strait in the Northwestern Subarctic Pacific. *Journal of Physical Oceanography*, *30*(6), 1137–1157.

Zhang, Z., Wang, W., & Qiu, B. (2014). Oceanic mass transport by mesoscale eddies. *Science*, *345*(6194), 322–324.